ELSEVIER

Experimental constraints on the partitioning of rhenium and some platinum-group elements between olivine and silicate melt

J.M. Brenan [a,*], W.F. McDonough [b], C. Dalpé [b,1]

[a] *Department of Geology, University of Toronto, 22 Russell Street, Toronto, ON, Canada M5S 3B1*
[b] *Department of Geology, University of Maryland, College Park, MD 20742, USA*

Abstract

We have performed partitioning experiments to assess the role of olivine in controlling the behavior of rhenium and the platinum group elements (PGEs) during basalt petrogenesis. Olivines were crystallized from an iron-bearing basalt at 1 bar (10^5 Pa) and log fO_2 of -2.6, -4.9 and -7.4 (FMQ $+4.3$, $+2$ and -0.5, respectively). In situ analyses of olivine and glass by laser ablation inductively coupled plasma mass spectrometry (LA-ICP-MS) reveal a homogeneous distribution of Ru, Rh, Pd, Re, and Pt, but significant Os heterogeneity at the μm scale. This latter behavior arises from the presence of undissolved Os micronuggets suspended in the melt, and included in olivine crystals. Olivine–melt partition coefficients (Ds) for Re and the PGEs follow the order: $D_{Rh} > D_{Ru} \gg D_{Pd} \sim D_{Re} \sim D_{Pt}$. With decreasing fO_2, Rh and Ru become more compatible, with maximum partition coefficients of ~ 2.6 and ~ 2, respectively, at log fO_2 of -4.9. In contrast, D values for Pd become smaller with decreasing fO_2, to a value of ~ 0.006 at log fO_2 of -7.4. Olivine–melt partitioning of Rh, Ru, Pd, Re and Pt derived from our experiments is confirmed by the behavior of these elements in lavas that have evolved by olivine fractionation. An elastic strain model predicts the olivine–melt partitioning of these elements, excepting our measured value of D_{Pt}, which is much lower. The fO_2 dependence on partitioning implies that at higher fO_2 some portion of PGEs exist in higher valence states than predicted from their solubility.
© 2003 Elsevier Science B.V. All rights reserved.

1. Introduction

Rhenium and the platinum group elements (PGEs) are valuable tracers of the processes responsible for small- and large-scale differentiation of the terrestrial planets. Despite this, much of our current knowledge of the phases that control the distribution of these elements is empirical, and subject to considerable uncertainty. With respect

* Corresponding author. Tel.: +1-416-978-0281;
Fax: +1-416-978-3938.
E-mail address: brenan@geology.utoronto.ca (J.M. Brenan).

[1] Present address: Royal Canadian Mounted Police, Forensic Laboratory Services, P.O. Box 8885, 1200 Vanier Parkway, Ottawa, ON, Canada K1G 3M8.

to magmatic processes, this problem is particularly acute, and although it is now well established that sulfide or alloy phases concentrate Re and the PGEs [1–6], the effect of primary liquidus minerals on their behavior remains obscure.

In mafic and ultramafic igneous systems, olivine is often considered a host for the IPGEs (iridium-PGEs: Ir, Os, Ru [1,3,7–13]). Conflicting data exist, however, and it is now demonstrated that Os and Ir do not always behave compatibly during olivine crystallization [2,14–16], and that the abundance of elements like Os and Ir in olivine separates can be extremely low and highly variable [17–19] – the latter suggesting that Os and Ir 'concentrations' may indeed be controlled by variable amounts of Os+Ir-rich inclusion phases. Whereas the IPGEs are compatible in olivine during mantle melting, Re and the PPGE (the palladium-PGEs: Pt, Rh, Pd) are incompatible [2,7,21].

Primitive mafic and ultramafic magmas from different tectonic settings are characterized by subchondritic IPGE/PPGE ratios [3], and superchondritic Re/Os values [22]. The latter feature is long-lived in crustal rocks and produces large differences in the Os isotopic composition of crustal and mantle rocks. Undepleted peridotites have near-chondritic relative abundances of Re and the PGEs [23], implying that the IPGEs are more compatible than Re and the PPGEs during partial melting. Accordingly, a detailed understanding of the relative olivine–melt partitioning of Re and the PGEs could shed significant light on the origin of the fractionation of these elements. To address this issue, we have performed olivine–silicate melt partitioning experiments for Re and the PGEs at oxygen fugacities approaching those of natural magmas.

2. Experimental techniques

Experiments were performed using a vertical tube furnace modified for control of fO_2 by gas mixing. Experiment temperatures were monitored using a ceramic-sheathed Pt–Pt10%Rh thermocouple calibrated against the melting point of gold. Control of gas mixtures was achieved using calibrated flow meters and furnace fO_2 was checked using the iron content of palladium coexisting with magnetite as a sliding redox sensor [24] and confirmed with a Y-doped zirconia oxygen probe (Australian Oxytrol Systems). We did experiments using pure CO_2, and two different CO–CO_2 mixtures, corresponding to log fO_2 of −2.6, −4.9 and −7.4 (FMQ +4.3, +2 and −0.5, respectively). These values are generally consistent with those calculated from the gas flow rates using the method of [25]. However, the theoretical log fO_2 of pure CO_2 at the conditions of our experiments is −3.3, and the higher value recorded in situ is probably the result of impurities in the gas phase.

Samples consisted of a synthetic basalt oxide mixture (modeled after the 401 diabase of [26]) plus Re or PGE metal added as a bead or powder, and the melt–metal mixture was held in open crucibles fabricated by drilling and coring single megacrysts of San Carlos olivine (SCO; 6.5 mm OD×2.5 mm ID×9 mm high and 5 mm hole depth). So as to maximize the concentration of Re and PGEs in run-product phases, only one or two metals were added to an experiment. Olivine crucibles were suspended in the furnace from the hooked end of a silica rod using a metal wire hanger wrapped around the top of the crucible, and up to three samples could be run together using multiple hooks fused to the end of the rod. Because the wire hanger invariably came into contact with the melt during an experiment, it was important to ensure that this communication did not result in substantial changes in the activity of metals within the melt, as a consequence of alloying. Hangers made from Rh or Pt30%Rh wire were used for experiments containing those metals, whereas palladium was chosen for samples containing Ru, Os and Re. Since Pd is largely immiscible with Ru and Os (∼3–9 wt% of Pd dissolves in Ru or Os, and vice versa) nearly constant activity of these metals is maintained during an experiment. The extent of Pd–Re solid solution is somewhat greater (∼16 wt% Re dissolves in Pd) however, so Re was added as a Re–Pd mixture that had been first annealed at 1400°C and log fO_2 of −9.6 for 48 h.

Experiments were executed by withdrawing the glass rod to the top of the furnace tube, then

sealing the furnace and commencing gas flow. After 20–30 min the sample was slowly lowered into the predetermined hot spot, and remained there for the experiment duration. The time–temperature history employed in experiments was designed to promote the growth of large olivine crystals from a melt whose Re or PGE content was homogeneous. To facilitate melt homogeneity, samples were first subject to an isothermal 'soak' at 1400°C, for durations of 24–192 h. After this, olivine growth was promoted by cooling to 1350°C at 60°/h, holding for 1 h, then cooling at 1°/h to 1335°C. Inasmuch as the trace element content of the olivine is largely acquired during growth (as opposed to much slower exchange by isothermal volume diffusion), the experiment was terminated at the end of the cooling step, which involved removing the bottom furnace seal and plunging the sample into an ice/water mixture.

The above-described experimental technique used starting compositions in which the initial melt contained negligible amounts of Re and PGEs. As a test for olivine–melt equilibrium, we also did some experiments in which the melt initially contained appreciable quantities of these elements. Given that metal solubilities increase substantially with increasing $f\mathrm{O}_2$, high metal contents

were accomplished by first subjecting melts to high-$f\mathrm{O}_2$ conditions. Experiment Ol+3+1.1 was initially soaked at 1400°C and log $f\mathrm{O}_2$ of −2.6 for 96 h, then the $f\mathrm{O}_2$ was lowered to log $f\mathrm{O}_2$ of −4.9 and the experiment was run with the same time–temperature history as other forward experiments. As a variation on this technique, experiment rev1 used a glass that was first presaturated in Os and Pd at 1400°C, log $f\mathrm{O}_2$ of −2.6 for 72 h. This glass was then extracted from the olivine crucible, ground, and packed in a fresh crucible with Os metal and hung with a Pd wire, then rerun as in forward experiments at log $f\mathrm{O}_2$ of −4.9. A summary of experiments is provided in Table 1.

3. Analytical techniques

3.1. Major elements

Run products were mounted in 2.54 cm diameter polycarbonate rounds and backfilled with epoxy. After setting, the mount was ground with SiC, and polished with alumina, then colloidal silica. Major element analysis was performed using the Cameca SX50 electron microprobe at the

Table 1
Summary of experiments

Expt. ID	PGE added	Holder[a]	$T_{superliq}$	$t_{superliq}$ (h)	T_{final}	log $f\mathrm{O}_2$	ΔFMQ[b]
Ol+3.1	Rh	SCO(Rh)	1400	24	1335	−2.6	4.3
Ol+3.3c	Rh	SCO(Rh)	1395	72	1334	−2.6	4.3
Ol+1.1	Rh	SCO(Rh)	1399	120	1336	−4.9	2.0
Ol+3.15	Pt/30%Rh	SCO(Pt/Rh)	1398	72	1335	−2.6	4.3
Ol+3.4b	Ru	SCO(Pd)	1398	135	1335	−2.6	4.3
Ol+1.3	Ru	SCO(Pd)	1398	96	1335	−4.9	2.0
Ol+3+1.1[c]	Ru	SCO(Pd)	1400	192	1335	−2.6/−4.9	4.3/2.0
Ol-1.2a	Os	SCO(Pd)	1397	135	1334	−7.4	−0.5
Ol-1.3a	Os	SCO(Pd)	1402	72	1339	−7.4	−0.5
Ol+1.2a	Os	SCO(Pd)	1399	120	1334	−4.9	2.0
rev1[d]	Os	SCO(Pd)	1399	121	1334	−4.9	2.0
Ol-1.2b	Pd-Re[e]	SCO(Pd)	1397	135	1334	−7.4	−0.5
Ol-1.3b	Pd-Re	SCO(Pd)	1402	72	1339	−7.4	−0.5

[a] SCO refers to San Carlos olivine crucible, metal in parentheses is the wire used to hang the crucible.
[b] log $f\mathrm{O}_2$ with respect to the FMQ buffer, calculated at the final run temperature.
[c] Sample run for 96 h at 1400°C, log $f\mathrm{O}_2$ of −2.6, then log $f\mathrm{O}_2$ of −4.9 for additional 96 h before cooling step.
[d] Starting material was Os and Pd-saturated glass synthesized at 1400°C, log $f\mathrm{O}_2$ of −2.6 for 72 h.
[e] Metal added was a pre-annealed Pd–Re mixture.

Table 2
Summary of glass analyses

Expt. ID	n^a	SiO_2	Al_2O_3	CaO	MgO	FeO	MnO	Na_2O	Total	Fe^{3+}/Fe^{2+} [b]	K_d Fe–Mg [c]
OI+3.1	16	51.79(0.2)	10.71(0.12)	9.81(0.12)	15.76(0.15)	10.64(0.22)	0.068(0.029)	0.76(0.08)	99.61	0.55	0.36
OI+3.3c	16	49.02(0.24)	9.94(0.08)	8.31(0.13)	15.39(0.15)	14.66(0.24)	0.104(0.03)	0.91(0.08)	98.58	0.56	0.34
OI+1.1	17	51.46(0.26)	10.62(0.08)	9.09(0.1)	15.65(0.07)	11.62(0.21)	0.146(0.025)	0.33(0.06)	98.92	0.16	0.34
OI+3.15	15	50.12(0.18)	9.07(0.09)	8.07(0.1)	15.92(0.11)	15.41(0.28)	0.151(0.031)	0.52(0.06)	99.32	0.55	0.36
OI+3.4b	16	50.81(0.3)	10.24(0.08)	9.08(0.09)	15.63(0.18)	12.61(0.23)	0.104(0.048)	0.54(0.07)	99.11	0.56	0.34
OI+1.3	15	53.33(0.21)	9.44(0.08)	8.64(0.10)	15.47(0.10)	12.72(0.21)	0.052(0.031)	0.56(0.08)	100.35	0.17	0.35
OI+3+1.1	15	51.53(0.17)	9.41(0.08)	7.81(0.1)	15.8(0.15)	14.59(0.25)	0.168(0.031)	0.31(0.05)	99.64	0.17	0.31
OI-1.2a	16	54.18(0.2)	11.43(0.09)	9.98(0.09)	15.64(0.12)	8.64(0.11)	0.091(0.025)	0.35(0.06)	100.43	0.05	0.34
OI-1.3a	16	52.32(0.16)	10.27(0.12)	9.29(0.1)	15.07(0.09)	12.23(0.17)	0.149(0.035)	0.56(0.07)	99.95	0.05	0.35
OI+1.2a	18	52.53(0.22)	10.74(0.08)	9.49(0.11)	15.28(0.13)	10.52(0.2)	0.104(0.027)	0.66(0.07)	99.34	0.17	0.35
rev1	17	51.47(0.21)	9.75(0.07)	8.71(0.12)	14.9(0.1)	13.33(0.15)	0.164(0.033)	0.71(0.06)	99.05	0.17	0.35
OI-1.2b	16	53.55(0.26)	10.8(0.1)	9.81(0.1)	15.19(0.13)	10.25(0.22)	0.113(0.04)	0.5(0.06)	100.27	0.05	0.34
OI-1.3b	16	52.19(0.27)	10.35(0.1)	9.57(0.12)	14.83(0.13)	12.12(0.2)	0.107(0.038)	0.43(0.07)	99.68	0.05	0.33

a n = number of points analyzed.
b Fe^{3+}/Fe^{2+} (molar) in melt calculated for T, fO_2 of experiment [28].
c Molar $(Fe^{2+}/Mg)_{olivine}/(Fe^{2+}/Mg)_{melt}$, equilibrium value is 0.28–0.33 [29].

University of Toronto. Two different electron beam conditions were used to analyze run-product silicates: 15 kV, 10 nA for glass and 20 kV, 50 nA for olivine. Standards for glass analyses were natural basalt (Si, Al, Mg, Fe, Ca), albite (Na), and bustamite (Mn), whereas olivine analyses used natural basalt (Al), bustamite (Ca, Mn), pentlandite (Ni) and synthetic olivine (Si, Mg, Fe). For all analyses, raw count rates were converted to concentrations using a modified ZAF data reduction scheme. Summaries of the major element composition of glass and olivine are provided in Tables 2 and 3, respectively.

3.2. Trace elements

Trace elements were determined using the laser ablation inductively coupled plasma mass spectrometry (LA-ICP-MS) facility in the Department of Geology at the University of Maryland. This system employs a frequency-quintupled Nd:YAG laser operating at 213 nm (UP213 from New Wave Research), coupled to an Element 2 (Thermo Finnigan MAT) magnetic sector ICP-MS. The ablation cell was flushed with He to enhance sensitivity [27]. Laser spot sizes ranged from ∼80 to ∼120 μm, with a 6 Hz laser repetition rate. A typical time-resolved analysis involved ∼20 s of background acquisition with the ablation cell being flushed with He, followed by laser ablation for 40 s, corresponding to a sampling depth of ∼40 μm (as measured in sample cross-section). A series of analyses were collected for each experiment run product, with the first and last three acquired on standards. Typically, four or more analyses were done on each phase. Standards employed were NIST 610 and 612 and 'in-house' standard JB-sulfide (a PGE-bearing NiS bead). The time-resolved spectra were processed off-line using a spreadsheet program to apply the background subtraction and calculation of absolute trace element abundances (modified version of LAMTRACE by Simon E. Jackson). Variations in ablation yields were corrected by reference to Ca, Mn or Ni concentrations measured by electron microprobe. The following isotopes were used to determine element concentrations reported in this study: ^{101}Ru, ^{103}Rh, ^{105}Pd, ^{185}Re,

Table 3
Summary of olivine analyses

Expt. ID	n	SiO_2	Al_2O_3	CaO	MgO	FeO	MnO	NiO	Total
SCO[a]	21	40.84(0.28)	0.03(0.01)	0.09(0.02)	49.65(0.77)	9.18(0.93)	0.14(0.02)	0.41(0.03)	100.34
Ol+3.1	15	40.87(0.23)	–	0.19(0.01)	51.18(0.28)	5.93(0.05)	0.05(0.01)	0.35(0.01)	98.56
Ol+3.3c	15	40.8(0.18)	–	0.17(0.01)	50.1(0.24)	7.63(0.16)	0.07(0.01)	0.379(0.009)	99.15
Ol+1.1	17	40.8(0.1)	–	0.18(0.01)	49.19(0.3)	9.21(0.54)	0.1(0.01)	0.355(0.016)	99.83
Ol+3.15	15	40.47(0.34)	0.05(0.01)	0.17(0.01)	49.31(0.43)	8.16(0.13)	0.11(0.01)	0.6(0.018)	98.85
Ol+3.4b	15	41.1(0.2)	–	0.18(0.01)	50.9(0.29)	6.54(0.31)	0.07(0.01)	0.392(0.012)	99.18
Ol+1.3	13	40.04(0.13)	0.04(0.01)	0.19(0.01)	47.84(0.12)	10.36(0.13)	0.11(0.01)	0.459(0.014)	99.01
Ol+3+1.1	15	40.46(0.21)	0.05(0.01)	0.16(0.01)	48.3(0.3)	10.44(0.31)	0.12(0.02)	0.368(0.013)	99.87
Ol-1.2a	15	41.01(0.27)	–	0.2(0.01)	50.11(0.48)	8.56(0.44)	0.07(0.01)	0.336(0.027)	100.29
Ol-1.3a	15	40.3(0.17)	0.04(0.01)	0.21(0.01)	46.94(0.14)	12.13(0.22)	0.13(0.01)	0.302(0.010)	100.05
Ol+1.2a	18	40.95(0.15)	–	0.2(0.01)	49.36(0.36)	8.95(0.42)	0.08(0.01)	0.38(0.018)	99.93
rev1	18	40.5(0.21)	–	0.2(0.01)	48.01(0.4)	11.14(0.44)	0.12(0.01)	0.354(0.016)	100.32
Ol-1.2b	15	40.72(0.26)	–	0.21(0.01)	48.91(0.33)	10.35(0.2)	0.09(0.01)	0.245(0.006)	100.52
Ol-1.3b	15	40.22(0.16)	–	0.22(0.01)	47.58(0.37)	11.81(0.43)	0.08(0.01)	0.219(0.008)	100.12

[a] Average of n different fragments from a mineral separate made from the San Carlos olivine used for the sample crucibles.

[192]Os, [194]Pt. Minimum detection limits for reported concentrations are calculated based on 2σ above the background count rate. As a check for interfering isobars, element concentrations were determined using multiple isotopes, when possible. A summary of the trace element content of glass and olivine is provided in Table 4.

4. Results and discussion

4.1. Textural observations

Olivine and metal alloy are the only crystalline phases present in the partitioning experiments. Olivines are relatively large (> 100 μm) and generally euhedral, with occasional glass inclusions (Fig. 1). In most cases, olivine crystals extend from the walls of the crucible, separated from the wall by a narrow septum, but isolated phenocrysts were also observed. The occurrence of metal alloy in all run products ensures that a constant Re and/or PGE activity was maintained over the course of an experiment.

4.2. Major element equilibrium

Electron microprobe analyses across individual olivines reveal them to be homogeneous, as the standard deviations of analyses are generally sim-

ilar to errors from counting statistics. Olivine compositions are also signficantly shifted in composition from the San Carlos olivine used as a container material (Table 3). Glass analyses from analytical traverses both across and down

Table 4
Trace element concentrations (ppm) and olivine/melt partition coefficients

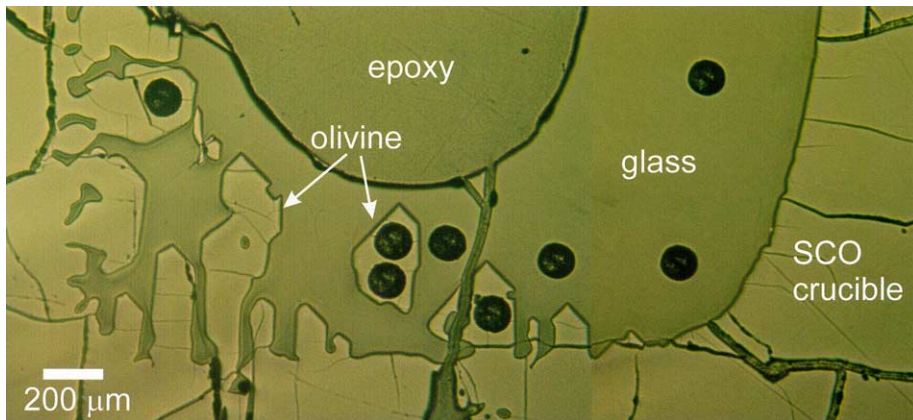| Element	Expt. ID	Olivine	Glass	D(Olivine/melt)
Ru	Ol+3.4b	4.07(0.40)	6.06(0.47)	0.67(0.08)
	Ol+1.3	0.33(0.03)	0.15(0.06)	2.19(0.89)
	Ol+3+1.1	0.21(0.07)	0.15(0.06)	1.40(0.73)
Rh	Ol+3.1	7.74(0.13)	4.00(0.22)	1.94(0.11)
	Ol+3.3c	6.43(0.37)	3.90(0.08)	1.65(0.10)
	Ol+1.1	1.13(0.08)	0.44(0.01)	2.59(0.19)
	Ol+3.15	2.99(0.19)	2.12(0.05)	1.41(0.10)
Pd	Ol+3.4b	1.39(0.16)	64.9(1.6)	0.021(0.003)
	Ol+1.3	0.23(0.07)	22.6(0.4)	0.010(0.003)
	Ol+3+1.1	0.41(0.05)	32.6(0.4)	0.013(0.002)
	Ol-1.2a	0.024(0.007)	3.48(0.11)	0.0069(0.0020)
	Ol-1.3a	0.016(0.005)	3.37(0.08)	0.0047(0.0015)
	Ol+1.2a	0.31(0.02)	21.4(0.6)	0.014(0.001)
	rev1	0.23(0.08)	19.6(0.4)	0.012(0.004)
	Ol-1.2b	0.024(0.002)	3.22(0.01)	0.0075(0.0006)
	Ol-1.3b	0.022(0.003)	3.62(0.02)	0.0061(0.0008)
Re	Ol-1.2b	< 0.002	2.43(1.21)	< 0.00082
	Ol-1.3b	< 0.002	1.98(0.87)	< 0.0010
Os	Ol-1.2a	< 0.011	< 0.010	–
	Ol-1.3a	< 0.021	< 0.010	–
	Ol+1.2a	< 0.013	< 0.006	–
	rev1	< 0.010	< 0.010	–
Pt	Ol+3.15	< 0.003	0.35(0.02)	< 0.009

Fig. 1. Reflected light photomicrograph of a portion of a sectioned and polished olivine crucible showing olivine and glass (experiment Ol+1.3). The dark, circular features are pits produced during laser ablation, cracks in olivine crucible were created during sample quenching. Newly grown euhedral olivines, having different Mg# compared to the SCO crucible, are projecting outward from the crucible walls.

the length of a run product reveal the same level of homogeneity as for olivines. This is also confirmed by the reproducibility of the minor element (Mn and Ni) content of crystals and glasses measured by LA-ICP-MS. In addition to phase homogeneity, phenocryst–melt equilibrium appears to be achieved, as judged by major and minor element partitioning systematics. Using the formulation of Klinic et al. [28], we calculated the FeO and Fe_2O_3 abundances in run-product glasses from the total FeO measured by electron microprobe. The olivine–melt FeO–MgO exchange coefficient was then calculated for coexisting phenocryst–glass pairs (Table 2). The resulting range of 0.31–0.36 (average of 0.34 ± 0.01) is somewhat elevated relative to the canonical value of 0.30 ± 0.02 [29], reflecting uncertainty in the calculated ferric–ferrous ratio. Olivine–melt partition coefficients for calcium are in agreement with the equilibrium value of 0.021 [30].

4.3. Trace element behavior

4.3.1. Phase homogeneity

Examples of time-resolved ICP-MS spectra for glass and olivine are provided in Figs. 2 and 3, respectively (olivine spectra for Pt and Re are not shown as these elements are at background levels). In general, both glasses and olivines show a homogeneous distribution of Re and PGEs, as judged by the uniform count rates for these elements with ablation time (= depth into sample). This result is true over the range of fO_2 investigated, despite decreases in metal content arising from reduced solubility at lower fO_2. The higher variation in time-resolved count rates in analyses from lower fO_2 experiments is the result of lower analytical precision arising from reduced signal intensity (e.g. Fig. 2A,E). Occasional alloy inclusions were encountered in analyses from runs containing Ru, Rh, Pd, Re and Pt, but they occurred as short-duration, high-intensity aberrations in an otherwise uniform time-resolved profile. Such features were avoided during the data reduction procedure.

Re and Os display some level of heterogeneity in run products. For the case of rhenium, although individual analyses show uniform time-resolved spectra (Fig. 2D), there is nearly a three-fold variation in the Re concentrations from different analysis spots. This probably reflects the presence of minor concentration gradients in the melt as a consequence of the volatility of Re at the T–fO_2 conditions of our experiments [31]. A similar level of heterogeneity is present in both Re-doped experiments, despite their different durations, which likely reflects the development of a steady-state gradient, inasmuch as both samples are saturated in Re alloy. Experiments containing osmium show a different sort of inhomogeneity.
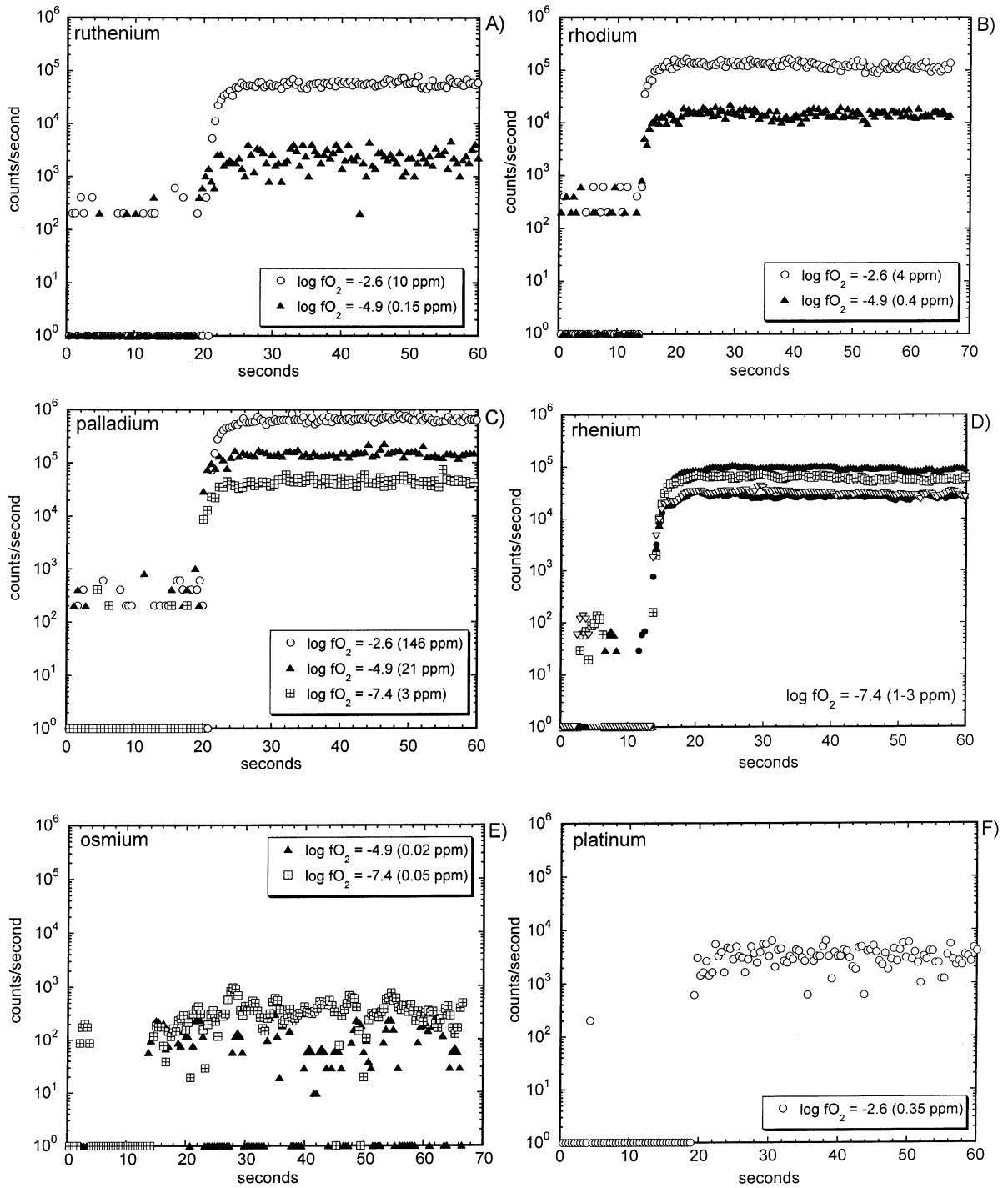
Fig. 2. Examples of LA-ICP-MS time-resolved spectra obtained from run-product glasses. In each case, instrument background is collected for 15–20 s, followed by laser ablation of the sample. Count rates corresponding to zero have been changed to one for the purposes of plotting on a log scale. Note the intensity variation in the spectra for osmium (panel E), which is due to the presence of micronuggets.
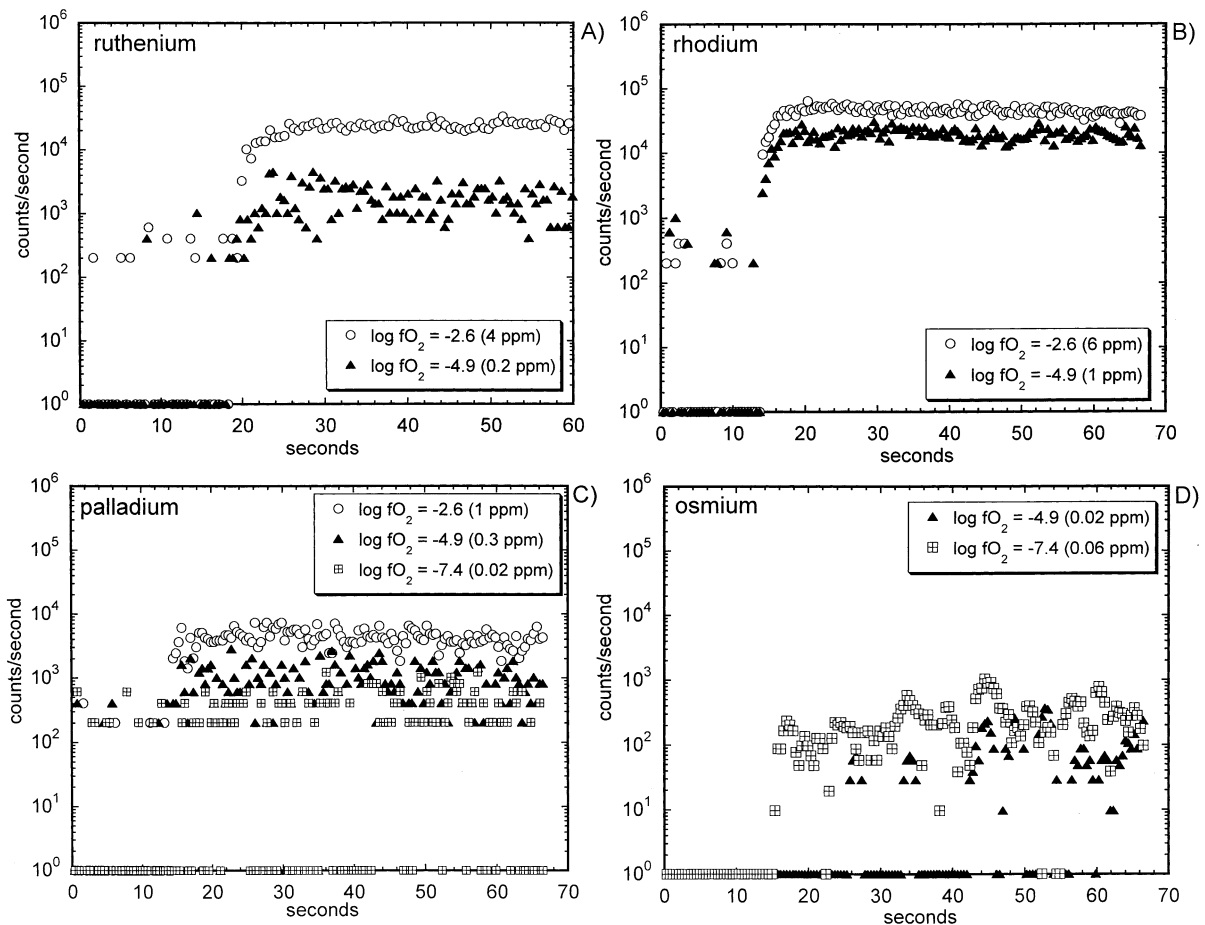
Fig. 3. LA-ICP-MS time-resolved spectra obtained from run-product olivines. Spectra for platinum and rhenium are not shown, as they are indistinguishable from background. As in Fig. 2E, the osmium spectrum in panel D shows intensity variation due to the presence of micronuggets. See the caption to Fig. 2 and the text for more details.

Although the signal intensity is relatively low, time-resolved spectra of both glass and olivine (Figs. 2E and 3D) show marked variations in Os content with time. This result was observed for phases produced at both fO_2s investigated (and similar behavior was seen for Ir in separate reconnaissance experiments). These spectra bear a striking similarity to those reported by Ertel et al. [32,33] for Rh, Pt and Re-saturated glasses equilibrated at low fO_2, with their interpretation being that the glasses contain undissolved alloy micronuggets. In addition to the observed intensity variations in time-resolved spectra, support for the occurrence of PGE alloy micronuggets stems from the results of detailed solubility studies in

which melt Pt and Rh concentrations appear to 'bottom out' at low levels (i.e. ∼100 ppb [32]), despite further reduction in the fO_2 of an experiment. It has thus been concluded that, although the intrinsic content of these elements in glass may further decrease, this effect is masked by the persistent presence of finely dispersed alloy particles (i.e. micronuggets). For the case of our partitioning experiments, the inhomogeneity observed in the spectra for olivine presumably reflects Os-alloy particles present in the melt and subsequently trapped by the growing olivine crystal. Inasmuch as there are clearly no constant intensity portions to the time-resolved spectra for Os, the intrinsic glass or olivine concentrations

of this element cannot be determined with confidence. Osmium concentrations reported in Table 4 correspond to the lowest apparent values (based on integrating the entire time-resolved spectra) of the spots measured, which places an upper bound on the intrinsic concentration for those phases.

4.3.2. Trace element equilibrium

The generally homogeneous distribution of Re and PGEs (except Os) within run products is a fundamental observation in support of phase equilibrium. However, a concern in these experiments is whether the PGE metal content of the melt has reached an equilibrium value such that olivines sample a uniform reservoir during growth. This concern arises because some studies show that metal–silicate melt equilibrium can be sluggish [4,32,33]. The lack of metal zonation in olivines is evidence of uniform metal content in the melt during growth. This is also supported by the reproduced partition coefficients for Ru and Pd by synthesis paths involving large changes in melt metal content (Fig. 4). Experiments in which the melt was first subject to high f_{O_2}, hence dissolving high metal concentrations (Ol+3+1.1 and rev1), then low f_{O_2}, in which the melt metal content decreased by $>10\times$, yielded similar melt metal contents (Table 4) and identical partition coefficients as the forward experiment done at lower f_{O_2} (Ol+1.3). In addition to reproducibility by different synthesis paths, we have also found that partition coefficients for Rh and Pd are the same for experiments in which the melt homogenization step lasted from 24 to 135 h (Fig. 4). Importantly, there is excellent agreement between the metal contents of melts produced in our experiments with those from previous solubility studies done at similar temperature and f_{O_2}, but involving Fe-free compositions (Table 5). The only exception to this is that we determined a maximum Os solubility of ~ 10 ppb, compared to the range of 40–200 ppb reported for previous experiments at 1400°C for samples analyzed by bulk techniques [34]. The discrepency could be the result of the higher temperatures employed in the latter experiments, or micronuggets sampled during bulk analysis. As a final note, we have also found that rhodium solubility
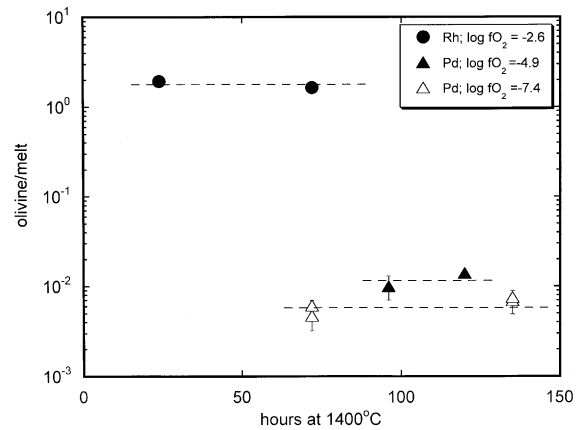

Fig. 4. Olivine–melt partition coefficients for Rh and Pd as a function of time spent at 1400°C (the melt homogenization step). Results are for experiments at the log f_{O_2} values indicated. Error bars are $\pm 1\sigma$, and based on the variation in element concentration for separate analysis spots. In some cases, the symbol size is larger than the error bar.

changes in a manner consistent with its activity in coexisting alloy. For experiments done at log f_{O_2} of -2.6, the Rh content of glass coexisting with pure Rh is ~ 4 ppm, whereas we measured ~ 2 ppm Rh in the glass coexisting with Pt–Rh alloy containing 45 mol% (30 wt%) Rh. Assuming unit activity coefficients, the predicted solubility is ~ 1.8 ppm, which is in excellent agreement with the measured value.

4.3.3. Olivine–melt partition coefficients

At log f_{O_2} of -2.6 and -4.9, Rh is the most compatible of the elements investigated, with D-values of 1.4–2.6. With decreasing f_{O_2}, Rh partition coefficients increase slightly (Fig. 5). At log f_{O_2} of -2.6, Ru is weakly incompatible in olivine ($D_{Ru} \sim 0.5$), but becomes compatible at log f_{O_2} of -4.9 ($D_{Ru} \sim 2$; Fig. 5). Pt is undetectable in olivines from the single high-f_{O_2} experiment done with this element, yielding a maximum D_{Pt} of ~ 0.01. Similarly, Re was below detection in olivine from both Re-bearing experiments, yielding $D_{Re} < 0.001$. Partition coefficients for Pd progressively decreased with decreasing f_{O_2}, ranging from ~ 0.03 at log f_{O_2} of -2.6 to ~ 0.005 at log f_{O_2} of -7.4 (Fig. 5). Thus, Pt, Re and Pd are moderately to strongly incompatible in olivine.

Table 5
Comparison of Re and PGE solubility data

Experiment ID	log fO_2	Metal[a]	Glass (ppm)	Solubility (ppm)	$T(°C)$[b]	Reference
Ol+3.1	−2.6	Rh$_{100}$	4.00(0.22)	2.35	1300	32
Ol+3.3c	−2.6	Rh$_{100}$	3.90(0.08)	2.35	1300	32
Ol+1.1	−4.9	Rh$_{100}$	0.44(0.01)	0.13	1300	32
Ol+3.15	−2.6	Rh$_{30}$	2.12(0.05)	2.35	1300	32
		Pt$_{70}$	0.35(0.02)	0.56	1300	32
Ol+3.4b	−2.6	Ru$_{89}$	6.06(0.47)	9.74	1300	41
		Pd$_{89}$	64.9(1.6)	59.6	1350	38
Ol+1.3	−4.9	Ru$_{89}$	0.15(0.06)	0.20	1300	41
		Pd$_{89}$	22.6(0.4)	14.2	1350	38
Ol+3+1.1	−4.9	Ru$_{89}$	0.15(0.06)	0.20	1300	41
		Pd$_{89}$	32.6(0.4)	14.2	1350	38
Ol-1.2a	−7.4	Os$_{97}$	< 0.010	0.04–0.2	1400	34
		Pd$_{96}$	3.48(0.11)	3.8	1350	38
Ol-1.3a	−7.4	Os$_{97}$	< 0.010	0.04–0.2	1400	34
		Pd$_{96}$	3.37(0.08)	3.8	1350	38
Ol+1.2a	−4.9	Os$_{97}$	< 0.006	0.04–0.2	1400	34
		Pd$_{96}$	21.4(0.6)	14.2	1350	38
rev1	−4.9	Os$_{97}$	< 0.010	0.04–0.2	1400	34
		Pd$_{96}$	19.6(0.4)	14.2	1350	38
Ol-1.2b	−7.4	Re$_{98}$	2.43(1.21)	3.7	1400	33
		Pd$_{84}$	3.22(0.01)	3.8	1350	38
Ol-1.3b	−7.4	Re$_{98}$	1.98(0.87)	3.7	1400	33
		Pd$_{84}$	3.62(0.02)	3.8	1350	38

[a] Composition of metal added (Rh or PtRh alloy), or resulting immiscible pairs based on the binary phase diagram. All compositions in wt%.
[b] Temperature at which solubility measurements were made.

In general, the partition coefficients we have measured are in very good agreement with values inferred from natural samples and other laboratory experiments. For example, based on correlations between PGE abundance and MgO content of komatiites, both Brugmann et al. [7] and Puchtel and Humayun [9] concluded that Ru is compatible in olivine (D_{Ru} = 1.7–1.8), whereas Pt and Pd are incompatible. Puchtel and Humayun [9] estimated values for D_{Pt} of 0.08 and D_{Pd} of 0.03. Similar behavior for Pd was documented by Barnes and Picard [1] for olivine–phyric basalts from Cape Smith, Quebec. This latter study also estimated a D_{Rh} of ~2, although it was suggested that small amounts of sulfide fractionation may have contributed to the compatibility of this element. Consistent with our maximum value for D_{Re} of ~0.001, Righter et al. [21] report an olivine–melt D_{Re} of < 0.005, although their experiments were for conditions ~100× more oxidizing (NNO) than those in this study. Similarly,

Walker et al. [15] estimated D_{Re} of 0.13 based on the composition of olivine separates and whole rocks for komatiites of Gorgona Island (Colombia).
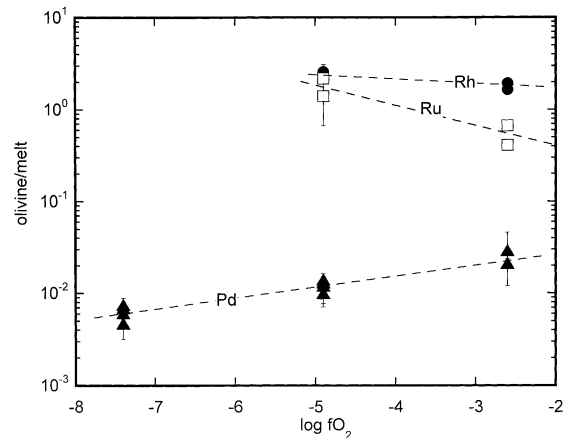
Fig. 5. Olivine–melt partition coefficients for Pd, Ru and Rh as a function of oxygen fugacity.

4.3.4. Origin of the variation in partition coefficients for Re and the PGEs

It is now well-established that mineral–melt partitioning of trace elements can be accurately modeled with knowledge of elastic moduli for the host mineral, the charge and ionic radius of the substituent ions, along with partitioning data for the major element these ions replace [35,36]. The basis for such models is that the energetics of partitioning is dominated by the amount of elastic strain associated with placing a cation on a particular crystallographic site when the radius of the cation differs from the optimal radius for that site. Beattie [35] and Purton et al. [37] demonstrated that olivine–melt partition coefficients for elements in VI-fold coordination adhere well to the elastic strain model, with values decreasing in proportion to their mismatch from the optimal radius for the octahedral site (r_o). We apply the Blundy and Wood [36] version of the elastic strain model to provide a framework for understanding the large variation in olivine–melt partition coefficients measured in this study. We recognize that there are several potential shortcomings to this exercise. First, the elastic strain model implicitly assumes that bond formation involving substituent cations is ionic and that 'crystal–field' effects are minimal. For Re and the PGEs, this latter assumption may not be fully justified, given d-shell electrons are involved in bonding. In addition, the oxidation states of Re and the PGEs at the temperature and fO_2 of our experiments have been estimated indirectly, using the variation in metal solubility with fO_2 in silicate melt. Based on such trends, at the fO_2 of our experiments Pd is predominantly in the univalent state [38], Ir, Rh, Pt are divalent [4,32,39,40], Ru and Os are trivalent [34,41], whereas Re is hexavalent [33]. With the exception of Re^{6+}, Ru^{3+} and Pt^{2+}, such oxidation states are unusually low [4], making the estimate of ionic radius difficult, as compounds containing Pd^{1+}, Ir^{2+}, Rh^{2+}, and Os^{3+} in octahedral coordination have not, to our knowledge, been characterized. We have estimated values by extrapolating data from Shannon and Prewitt [42,43], assuming a linear relation between ionic radius and charge.

According to the Blundy–Wood model, the re-lation between the partition coefficient, D_i, for a particular cation of radius r_i, is expressed as:

$$D_i = D_o \exp(-4\pi E N_a (r_o/2(r_o-r_i)^2$$

$$-1/3(r_o-r_i)^3/RT) \tag{1}$$

in which D_o is the value of the partition coefficient corresponding to the optimal radius for substitution into the olivine octahedral site, r_o, and E is the Young's modulus for the site. The optimal radius for the olivine octahedral site was calculated by Beattie [35] to be 0.058 nm using the volume between 'just touching' spherical oxygen atoms at the edges of an octahedron, and is the value adopted here (note this estimate is somewhat lower than the value of 0.063 nm used by Purton et al. [37]). Wood and Blundy [44] have shown that D_o varies systematically with cation charge, with the functional form being:

$$\ln D_o \approx 6.95 \times 10^5 (Z_c-Z_o)^2/\varepsilon' r_S \tag{2}$$

where Z_c and Z_o correspond to the charges on the substituting trace cation and the major cation occupying the site, respectively, ε' is the dielectric constant of the mineral, and r_S is the radius of the strained zone around the trace substituent cation. This model thus allows one to predict the partition coefficient for a particular element given the cation radius and values of D_o and E for that particular cation charge. The data obtained in our study are only sufficient to determine D_o for 2+ cations, so to obtain values of D_o for cations having other charges, we have fit the functional form of Eq. 2 to values of D_o regressed from olivine–melt partitioning data of previous work using Eq. 1, and results are shown in Fig. 6. With the fit parameters derived from those data, we can thus predict the value of D_o for a particular cation charge based on the value of D_o regressed from our divalent partitioning data. Values of E for 1+, 3+ and 4+ cations were regressed from previously published olivine–melt partitioning data [35,45,46] using Eq. 1.

A comparison between measured partition coefficients and those calculated using the Blundy–Wood model is shown in Fig. 7. Partition coefficients for Rh, Pt and Ru determined at log fO_2 of −2.6 plot significantly below the model curves for
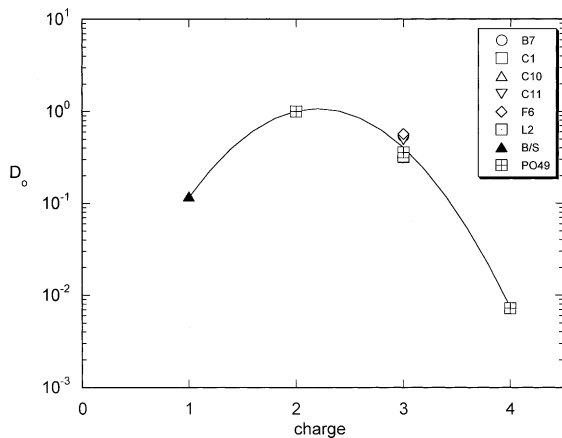
Fig. 6. D_o as a function of cation charge determined by regressing the experimental data of Beattie ([35]; experiments B7-L2), Brenan et al. ([45]; experiment B/S) and Kennedy et al. ([46]; experiment PO49) using Eq. 1. All values of D_o were normalized to D_o^{2+}, then fit to a single curve having the form of Eq. 2 (solid curve).

di- and trivalent cations, whereas those measured at log fO_2 of −4.9 are in good agreement with the theoretical predictions. The partition coefficient for Pd is higher than anticipated by the Blundy–Wood model for 1+ cations at log fO_2 of −2.6 and −4.9, but at −7.4, experimental and model values are in very good agreement. Due to a lack of data to constrain the value of E for 6+ cations, we have not calculated a partitioning curve for comparison to our Re partitioning results. However, the trend of decreasing D-value with increasing cation charge is clear from the position of the model 4+ curve, and consistent with the overall incompatibility of Re in olivine.

The general correspondence between our partitioning data for Rh, Ru and Pd at log fO_2 of less than −2.6 and the values predicted from the elastic strain model suggests that our choice of valence states for these elements is correct for those conditions. At log fO_2 of −2.6, the sense of deviation between measured and modeled partition coefficients is consistent with higher valence states than that assumed for metal solubility data. The reduction in Pd partition coefficient with decreasing fO_2 is reasonable if Pd is predominantly 2+ (which would be most compatible in the olivine structure) at log fO_2 of −2.6 and mostly 1+ at log fO_2 of −7.4. This change in oxidation state was

previously suggested by Borisov et al. [38] as a means to best model their solubility data, although Pd^{1+} is considered to be the dominant oxidation state over the fO_2 range we investigated. If Rh and Ru have higher valence than 2+ and 3+, respectively, at log fO_2 of −2.6, then it is expected that partition coefficients for these elements would fall below the model 2+ and 3+ curves, as higher valence states are less compatible, as demonstrated by the elastic strain modeling. The very low partition coefficient for Pt is surprising, as the Pt solubility data of Ertel et al. [32] are adequately modeled assuming Pt^{2+} as the dominant oxidation state, although these authors also suggested some Pt^{4+} could be present at the highest fO_2s investigated (log fO_2 of −0.69 and 0), which has been confirmed spectroscopically [47]. As such, we expected D_{Pt} to be about 1/3 D_{Rh}, given the larger ionic radius of Pt in the 2+ oxidation state. The incompatibility of Pt in olivine that we have documented suggests that valence states higher than 2+ are present at log fO_2 of −2.6. If we assume an ionic radius corresponding to Pt^{4+} in VI-fold coordination we obtain good correspondence between the measured value of D_{Pt} and that predicted for 4+ cations (Fig. 7), thus supporting this contention. The presence of abundant Pt micronuggets found in the glass produced in reconnaissance experiments done at lower fO_2 precludes the measurement of Pt partition coefficients at those conditions. Thus, information bearing on the extent to which the compatibility of Pt increases with decreasing fO_2 awaits future work.

Given the predictive capability of the elastic strain model for Ru, Rh and Pd partitioning, it is useful to speculate on the behavior of the other PGEs for which we were unable to measure partition coefficients: Os and Ir. The major caveat for these predictions is that the primary valence state for these elements is accurately predicted by the metal solubility measurements described previously. In VI-fold coordination, we estimate that trivalent Os has the same ionic radius as Ru (0.068 nm), so that $D_{Os} \sim D_{Ru}$. Divalent Ir has an estimated ionic radius of 0.074 nm, which is larger than Rh (0.072 nm), and based on the trend in ionic radius with D, we predict that partition
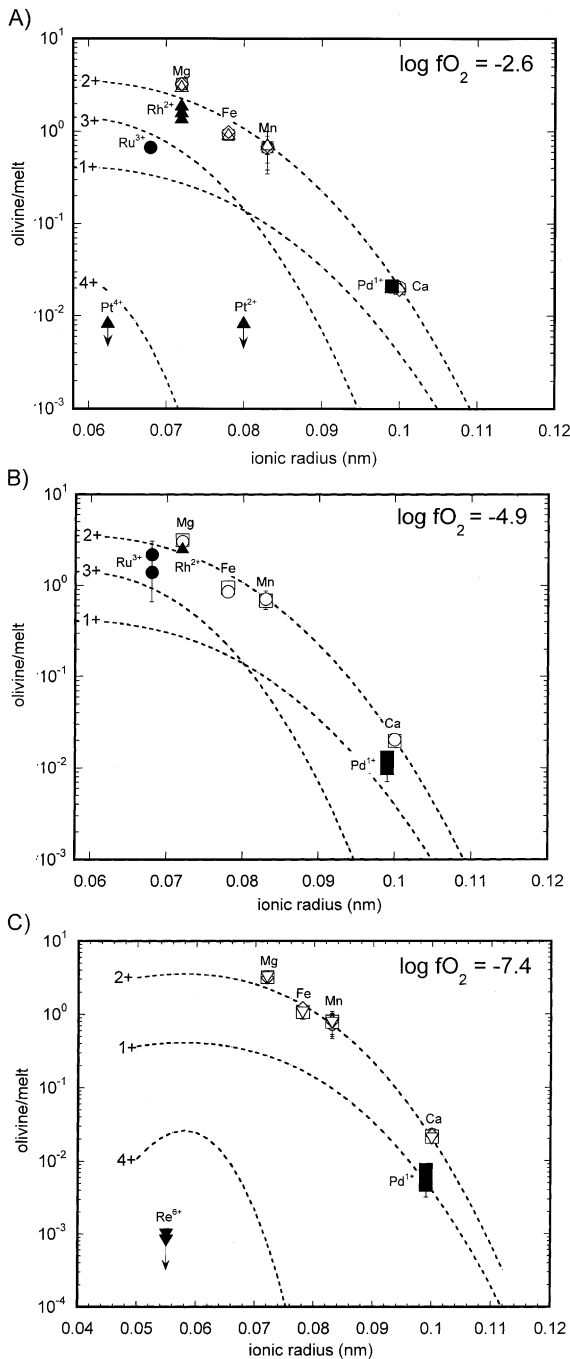
Fig. 7. Comparison of olivine–melt partition coefficients predicted using the lattice-strain model of Blundy and Wood ([36]; dashed curves) and those measured in this study at log fO_2 of (A) −2.6, (B) −4.9 and (C) −7.4. Ionic radii are for VI-fold coordination and the indicated cation charge.

coefficients will obey the relation: $D_{Rh} \sim 1.2D_{Ir}$. Thus, both Os and Ir are predicted to be compatible in olivine, with partition coefficients of ~ 2 estimated for each, based on values of D_{Ru} and D_{Rh} measured in this study. Brugmann et al. [7] and Puchtel and Humayen [9] estimated values for D_{Os} of 1.2 and 1.8 and for D_{Ir} of 0.8 and 1.8, respectively, in komatiites, which are similar to the values derived in this study. Hart and Ravizza [13] calculated a D_{Os} of 20 from olivine separates combined with a whole-rock lava composition, which suggests a much higher degree of compatibility than we have inferred. In contrast, both Walker et al. [16] and Burton et al. [20] suggested that Os is incompatible in olivine, with D_{Os} of < 0.1, as determined from mineral separate–whole-rock relations. Given this disparity between our estimate for D_{Os} and values derived from some natural samples, we view our estimated value with caution, and direct measurements of D_{Os} are a high priority for future research.

4.4. Implications for Re and PGE behavior during melting

The partitioning of PGEs between other ferromagnesian silicates and silicate melt is poorly known, with the exception of the D_{Os} of 0.08 measured for clinopyroxene [48] at high, but unbuffered fO_2. Previous work has shown that spinel-structured minerals (spinel, magnetite) have large partition coefficients for Rh and Ru ($D_{Ru,Rh} > 100$), and exclude Pd [24,49]. Similar behavior has been inferred for chromite [9]. Such partitioning is similar to olivine, although less extreme in the extent of fractionation. Partition coefficients for the PGEs between immiscible silicate and sulfide melt (e.g. [50,51] are uniformly high (10^3–10^4), with no systematic variation in values between the IPGEs and the PPGEs [51]. Thus, we may anticipate that, for the case of melting of a sulfide-free mantle source, liquids will be slightly depleted, relative to the source, in Os, Ir, Ru and Rh, and show moderate relative enrichments in Pt and Pd. Higher degrees of melting will result in smaller relative fractionation of Pt and Pd from the other PGEs. Such behavior is similar to that found for komatiites, which typically have

Os, Ir and Ru abundance levels slightly less than values estimated for primitive mantle, with Pt and Pd being at or above primitive mantle levels (e.g. [7,9]). In contrast to komatiites, PGE abundances in mid-ocean ridge basalts (MORB) and ocean island basalts (OIB) are depleted 10- to 100-fold relative to upper mantle samples (e.g. [3,22,52]), indicating that these elements are uniformly compatible during melting or crystallization. Given mantle sulfur abundances in the range of 150–330 ppm [53], combined with the relatively low degrees of melting inferred for MORB and OIB (circa < 15%), it is likely that such magmas are sulfide-saturated in their source [54]. Such magmas still show a small to moderate fractionation of Os, Ir, Ru and Rh relative to Pt and Pd, which could be controlled by olivine (and possibly chromite) in the source, or result from low-pressure olivine fractionation.

In addition to the incompatibility of Re in olivine reported in this study, similar behavior has been documented for orthopyroxene and clinopyroxene, with D_{Re} ranging from 0.04 [48] to 0.3–0.4 [21]. In contrast, Righter and Hauri [55] found that Re was moderately compatible in garnet, with D_{Re} ranging from 1.4 to 4.8. During melting of a sulfide-free mantle source, we would therefore expect Re to be moderately to strongly enriched in the melt, relative to Os, with the extent of enrichment dependent on the amount of residual garnet. Sattari et al. [56] measured a D_{Re} of 4×10^4 for sulfide–silicate melt partitioning, which is at least three times lower than values measured for Os in the same experiments. Therefore, melts generated in the presence of residual sulfide will also have higher Re/Os than their source. The high Re/Os ratio in MORB and OIB, relative to likely mantle source rocks, and the low $^{187}Os/^{188}Os$ in peridotites [57] demonstrates that Re is more incompatible than Os during melting of the upper mantle, in agreement with behavior predicted from experimental studies.

5. Summary and conclusions

This study demonstrates the utility of employing LA-ICP-MS to characterize the mineral–melt partitioning behavior of the highly siderophile noble metals. Owing to the generally low solubility of these elements in silicate melts, it is necessary to conduct experiments at metal saturation levels, making it essential that time-resolved analytical techniques be used to avoid inclusion phases. We have shown that olivine has a strong preference for Ru and Rh relative to Pt, Pd and Re, results which are consistent with the behavior of these elements in natural samples. The elastic strain models developed by Beattie [35] and Blundy and Wood [36] account for most of this behavior, except for Pt, which is more incompatible than predicted. The observed variation in olivine–melt partition coefficients for Rh, Ru and Pd with fO_2 can be accounted for by some change in the predominant valence state of these elements, with higher values than predicted from solubility measurements present at the highest fO_2s. Measured and predicted partitioning behavior for phases likely to be residual during mantle melting is consistent with the sense of fractionation of Re and the PGEs in mantle-derived magmas and peridotite residua, suggesting that olivine–melt partitioning exerts a strong control on siderophile element fractionation in natural magmatic systems.

References

[1] S.-J. Barnes, C.P. Picard, The behaviour of platinum-group elements during partial melting, crystal fractionation, and sulphide segregation: An example from the Cape Smith Fold Belt, northern Quebec, Geochim. Cosmochim. Acta 57 (1993) 79–87.

[2] W.D. Maier, S.-J. Barnes, Platinum-group elements in silicate rocks of the Lower, Critical and Main Zones at Union Section, Western Bushveld Complex, J. Petrol. 40 (1999) 1647–1671.

[3] S.J. Barnes, A.J. Naldrett, M.P. Gorton, The origin of the fractionation of the platinum group elements in terrestrial magmas, Chem. Geol. 53 (1985) 303–323.

[4] H.St.C. O'Neill, D. Dingwell, A. Borisov, B. Spettel, H. Palme, Experimental petrochemistry of some highly siderophile elements at high temperatures, and some implications for core formation and the mantle's early history, Chem. Geol. 120 (1995) 255–273.

[5] C.L. Peach, E.A. Mathez, Constraints on the formation of platinum-group element deposits in igneous rocks, Econ. Geol. 91 (1996) 439–450.

[6] D.C. Peck, R.R. Keays, R.J. Ford, Direct crystallization of refractory platinum-group element alloys from bonitic magmas: Evidence from western Tasmania, Aust. J. Earth Sci. 39 (1992) 373–387.

[7] G.E. Brugmann, N.T. Arndt, A.W. Hofmann, H.J. Tobschall, Noble metal abundances in komatiite suites from Alexo, Ontario, and Gorgona Island, Colombia, Geochim. Cosmochim. Acta 51 (1987) 2159–2169.

[8] I.S. Puchtel, M. Humayen, Platinum group elements in Kostomuksha komatiites and basalts: Implications for oceanic crust recycling and core-mantle interaction, Geochim. Cosmochim. Acta 64 (2000) 4227–4242.

[9] I.S. Puchtel, M. Humayen, Platinum group element fractionation in a komatiitic basalt lava lake, Geochim. Cosmochim. Acta 65 (2001) 2979–2994.

[10] J.H. Crockett, Geochemistry of the platinum-group elements, Can. Inst. Min. Metall. Spec. Issue 23 (1981) 47–64.

[11] I.O. Oshin, J.H. Crocket, Noble metals in Thetford Mines ophiolites, Quebec. Part 1. Distribution of gold, iridium, platinum, and palladium in the ultramafic and gabbroic rocks, Econ. Geol. 77 (1982) 1556–1570.

[12] R.R. Keays, (1982) Palladium and iridium in komatiites and associated rocks, application to petrogenetic problems, in: N.T. Arndt, E.G. Nisbet (Eds.), Komatiites, Allen, London, 1982, pp. 435–458.

[13] S.R. Hart, G.E. Ravizza, Os partitioning between phases in lherzolite and basalt, in: Earth Processes: Reading the Isotopic Code, AGU Monogr. 95 (1996) 123–133.

[14] R.J. Walker, S.B. Shirey, O. Stecher, Comparative Re-Os, Sm-Nd and Rb-Sr isotope and trace element systematics for Archean komatiite flow from Munro Township, Abitibi Belt, Ontario, Earth Planet. Sci. Lett. 87 (1988) 1–12.

[15] R.J. Walker, L.M. Echeverria, S.B. Shirey, M.F. Horan, Re-Os isotopic constraints on the origin of volcanic rocks, Gorgona Island, Colombia: Os isotopic evidence for ancient heterogeneities in the mantle, Contrib. Mineral. Petrol. 107 (1991) 150–162.

[16] R.J. Walker, M. Storey, A.C. Kerr, J. Tarney, N.T. Arndt, Implication of [187]Os isotopic heterogeneities in a mantle plume: Evidence from Gorgona island and Curaçao, Geochim. Cosmochim. Acta 63 (1999) 713–728.

[17] R.H. Mitchell, R.R. Keays, Abundance and distribution of gold, palladium and iridium in some spinel and garnet lherzolites: Implication for the nature and origin of precious metal-rich intergranular components in the upper mantle, Geochim. Cosmochim. Acta 45 (1981) 2425–2442.

[18] J.P. Lorand, R.R. Keays, J.L. Bodinier, Copper and noble metal enrichments across the lithosphere-asthenosphere boundary of mantle diapirs: evidence from the Lanzo lherzolite massif, J. Petrol. 34 (1993) 1111–1140.

[19] D.G. Pearson, S.B. Shirey, R.W. Carlson, F.R. Boyd, N.P. Pokhilenko, N. Shimizu, Re-Os, Sm-Nd, and Rb-Sr isotope evidence for thick Archean lithospheric mantle beneath the Siberian craton modified by multistage metasomatism, Geochim. Cosmochim. Acta 59 (1995) 959–977.

[20] K.W. Burton, A. Gannoun, J-L. Birk, C.J. Allegre, P. Schiano, R. Clocchiatti, O. Alard, The compatibility of rhenium and osmium in natural olivine and their behaviour during mantle melting and basalt petrogenesis, Earth Planet. Sci. Lett. 198 (2002) 63–76.

[21] K. Righter, C.J. Capobianco, M.J. Drake, Experimental constraints on the partitioning of Re between augite, olivine, melilite and silicate liquid at high oxygen fugacities (>NNO), EOS Trans. AGU 76 (1995) F698.

[22] S.B. Shirey, R.J. Walker, The Re-Os isotope system in cosmochemistry and high temperature geochemistry, Annu. Rev. Earth Planet. Sci. 26 (1998) 423–500.

[23] J.W. Morgan, G.A. Wandless, R.K. Petrie, A.J. Irving, Composition of the Earth's upper mantle - I. Siderophile trace elements in ultramafic nodules, Tectonophysics 75 (1981) 47–67.

[24] C.H. Capobianco, R.L. Hervig, M. Drake, Experiments on crystal/liquid partitioning of Ru, Rh and Pd for magnetite and hematite solid solutions crystallised from silicate melt, Chem. Geol. 113 (1994) 23–43.

[25] V. Kress, Thermochemistry of sulfide liquids. I. The system O-S-Fe at 1 bar, Contrib. Mineral. Petrol. 127 (1997) 176–184.

[26] P.L. Roeder, I. Reynolds, Crystallisation of chromite and chromium solubility in basaltic melts, J. Petrol. 32 (1991) 909–934.

[27] S.M. Eggins, L.P.J. Kinsley, J.M.M. Shelley, Deposition and element fractionation processes during atmospheric pressure laser sampling for analysis by ICPMS, Appl. Surf. Sci. 127–129 (1998) 278–286.

[28] A. Klinic, I.S.E. Carmichael, M.L. Rivers, R.O. Sack, The ferric/ferrous ratio of natural silicate liquids equilibrated in air, Contrib. Mineral. Petrol. 83 (1983) 136–140.

[29] P.L. Roeder, R.F. Emslie, Olivine-liquid equilibrium, Contrib. Mineral. Petrol. 29 (1970) 275–289.

[30] A.J.G. Jurewicz, E.B. Watson, Cations in olivine, Part 1: Calcium partitioning and calcium-magnesium distribution between olivines and coexisting melts, with petrological applications, Contrib. Mineral. Petrol. 99 (1988) 176–185.

[31] A. Borisov, J.H. Jones, An evaluation of Re, as an alternative to Pt, for the 1 bar loop technique: An experimental study at 1400°C, Am. Min. 84 (2000) 1528–1534.

[32] W. Ertel, H.St.C. O'Neill, P.J. Sylvester, D.B. Dingwell, Solubilities of Pt and Rh in haplobasaltic silicate melt at 1300°C, Geochim. Cosmochim. Acta 63 (1999) 2439–2449.

[33] W. Ertel, H.St.C. O'Neill, P.J. Sylvester, D.B. Dingwell, B. Spettel, The solubility of rhenium in silicate melts: Implications for the geochemical properties of rhenium at high temperatures, Geochim. Cosmochim. Acta 65 (2001) 2161–2170.

[34] A. Borisov, R.J. Walker, Os solubility in silicate melts: New efforts and results, Am. Min. 85 (2000) 912–917.

[35] P. Beattie, Systematics and energetics of trace-element partitioning between olivine and silicate melts: implications for the nature of mineral/melt partitioning, Chem. Geol. 117 (1994) 57–71.

[36] J. Blundy, B.J. Wood, Prediction of crystal-melt partition coefficients from elastic moduli, Nature 372 (1994) 452–454.

[37] J.A. Purton, J.D. Blundy, N.L. Allan, Computer simulation of high-temperature, forsterite-melt partitioning, Am. Min. 85 (2000) 1087–1091.

[38] A. Borisov, H. Palme, B. Spettel, Solubility of palladium in silicate melts: Implications for core formation in the Earth, Geochim. Cosmochim. Acta 58 (1994) 705–716.

[39] A. Borisov, H. Palme, Solubility of iridium in silicate melts: New data from experiments with $Ir_{10}Pt_{90}$ alloys, Geochim. Cosmochim. Acta 59 (1995) 481–485.

[40] A. Borisov, H. Palme, Experimental determination of the solubility of Pt in silicate melts, Geochim. Cosmochim. Acta 61 (1997) 4349–4357.

[41] A. Borisov, K. Nachtweyh, Ru solubility in silicate melts: experimental results in oxidizing region, Lunar and Planetary Science XXIX, 1998, Abstract No. 1320.

[42] R.D. Shannon, C.T. Prewitt, Effective ionic radii in oxides and fluorides, Acta Cryst. B 25 (1969) 925–946.

[43] R.D. Shannon, C.T. Prewitt, Revised values of effective ionic radii, Acta Cryst. B 26 (1970) 1046–1048.

[44] B.J. Wood, J.D. Blundy, The effect of cation charge on crystal-melt partitioning of trace elements, Earth Planet. Sci. Lett. 188 (2001) 59–71.

[45] J.M. Brenan, E. Neroda, C.C. Lundstrom, H.F. Shaw, F.J. Ryerson, D.L. Phinney, Behaviour of boron, beryllium and lithium during melting and crystallization: constraints from mineral-melt partitioning experiments, Geochim. Cosmochim. Acta 62 (1998) 2129–2141.

[46] A.K. Kennedy, G.E. Lofgren, G.J. Wasserburg, An experimental study of trace element partitioning between olivine, orthopyroxene and melt in chondrules: equilibrium values and kinetic effects, Earth Planet. Sci. Lett. 115 (1993) 177–195.

[47] F. Farges, D.R. Neuville, G.E. Brown, Structural investigation of platinum solubility in silicate glasses, Am. Min. 84 (1999) 1562–1568.

[48] E.B. Watson, D. Ben Othman, J.-M. Luck, A.W. Hofmann, Partitioning of U, Pb, Cs, Yb, Hf, Re and Os between chromian diopsidic pyroxene and haplobasaltic liquid, Chem. Geol. 62 (1987) 191–208.

[49] C.H. Capobianco, M. Drake, Partitioning of ruthenium, rhodium, and palladium between spinel and silicate melt and implications for platinum-group element fractionation trends, Geochim. Cosmochim. Acta 54 (1990) 869–874.

[50] M.E. Fleet, J.H. Crocket, W.E. Stone, Partitioning of platinum-group elements (Os, Ir, Ru, Pt, Pd) and gold between sulfide liquid and basalt melt, Geochim. Cosmochim. Acta 60 (1996) 2397–2412.

[51] C.L. Peach, E.A. Mathez, R.R. Keays, S.J. Reeves, Experimentally determined sulfide melt-silicate melt partition coefficients for iridium and palladium, Chem. Geol. 117 (1994) 361–377.

[52] Y. Tatsumi, K. Oguri, G. Shimoda, The behaviour of platinum-group elements during magmatic differentiation in Hawaiian tholeiites, Geochem. J. 33 (1999) 237–247.

[53] J.P. Lorand, Are spinel lherzolite xenoliths representative of the abundance of sulfur in the mantle?, Geochim. Cosmochim. Acta 54 (1990) 1487–1492.

[54] J.A. Mavrogenes, H.St.C. O'Neill, The relative effects of pressure, temperature and oxygen fugacity on the solubility of sulfide in mafic magmas, Geochim. Cosmochim. Acta 63 (1999) 1173–1180.

[55] K. Righter, E.H. Hauri, Compatibility of rhenium in garnet during mantle melting and magma genesis, Science 280 (1998) 1737–1741.

[56] P. Sattari, J.M. Brenan, I. Horn, W.F. McDonough, Experimental constraints on the sulfide- and chromite-silicate melt partitioning behavior of rhenium and platinum-group elements, Econ. Geol. 97 (2002) 385–398.

[57] T. Meisel, R.J. Walker, A.J. Irving, J.P. Lorand, Osmium isotopic compositions of mantle xenoliths: A global perspective, Geochim. Cosmochim. Acta 65 (2001) 1311–1323.